Experimental and Computational Investigation for In-Line Boundary Layer Ingestion

Lucas L. Kob[1], John J. Doherty[2], and David M. Birch[3]
University of Surrey, Guildford, Surrey, United Kingdom, GU2 7XH

James Robson
Aerodynamics; Analysis, Modelling & Simulation,
QinetiQ Ltd, Farnborough, United Kingdom

The aerodynamic characteristics of an aft-body, in-line mounted, boundary layer ingesting, electric ducted fan, propulsion installation system has been investigated through experimental and computational analysis. A modular wind-tunnel model allows variation in the geometry of the propulsion installation system to be assessed, in combination with fan speed. Various experimental measurement techniques, including LDA, seven-hole-probe and surface pressures are employed. The propulsion installation system has also been investigated using RANS CFD and comparison with experimental data is presented. An investigation of the boundary conditions for efficiently representing the fan in CFD is described. Initial results show reasonably good agreement between CFD and experiment, in terms of velocity profiles and surface pressures, but highlight remaining differences for cases exhibiting flow separation.

Nomenclature

BLI	=	boundary layer ingestion
C_p	=	pressure coefficient ($^{p - p_\infty}/_{q_\infty}$)
CFD	=	computational fluid dynamics
D	=	model diameter
EDF	=	electric ducted fan
ESC	=	electric speed controller
FB	=	force balance
FF	=	flow field
H	=	shape factor
L	=	boat-tail length
LDA	=	laser Doppler anemometry
LE	=	leading edge
q_∞	=	free stream tunnel dynamic pressure ($1/2\ \rho_\infty U_\infty^2$)
RPM	=	revolutions per minute
U	=	local flow velocity ($\sqrt{u^2 + v^2 + w^2}$)
U_∞	=	free stream velocity
u,v,w	=	velocity components in axial-, tangential-, and radial-direction
ρ_∞	=	free stream density
β	=	aft-body boat-tail angle
δ^*	=	boundary layer displacement thickness
θ	=	boundary layer momentum thickness

[1] PhD Candidate, l.kob@surrey.ac.uk, Student Member AIAA
[2] Head of Centre for Aerodynamics and Environmental Flow, john.doherty@surrey.ac.uk, AF AIAA
[3] Senior Lecturer, Department of Mechanical Engineering Sciences, Senior Member AIAA

I. Introduction

Closely or fully embedded propulsion systems offer potential for compact air-vehicle designs, where removal of separate engine mounting components can result in reduced weight and wetted area. Furthermore, a beneficial interaction between an airframe and a propulsion system with associated boundary layer ingestion (BLI), can potentially have significant aerodynamic benefits [1]. In the field of marine propulsion beneficial body propulsor interactions have been acknowledged, studied and applied since the mid-19th century [2] [3] [4] [5]. Beneficial aerodynamic effects were first observed and described by Fage [6] [7] and Glauert [8] in the early 20th century. The topic has received increased attention since the early 1990's, when Smith [1] introduced an alternative metric to quantify the aerodynamic benefit of BLI as the power savings coefficient (PSC),

$$PSC = \frac{P_S - P_{S,BLI}}{P_S} \tag{1}$$

in which shaft power without the use of BLI (P_S) is put in relation to the shaft power of a BLI utilizing configuration ($P_{S,BLI}$). Moreover, he constitutes the effectiveness of BLI to be a function of boundary layer characteristics, specifically the shape factor (H),

$$H = \frac{\delta^*}{\theta} \tag{2}$$

which is defined by the ratio of displacement thickness (δ^*) and momentum thickness (θ). For the ingestion of boundary layer flow with a particularly high shape factor he stated potential performance improvements in the order of 20% when operated downstream of an axisymmetric air-vehicle. BLI has since been proposed for numerous air-vehicle concepts with the aim of increasing performance efficiency [9] [10] [11]. Traditional thrust-drag accounting however cannot be applied for such configurations as the complex aerodynamic interactions between propulsor and body void the separate treatment of thrust and drag. Many conceptual studies superimpose the propulsion system's performance on independently calculated boundary layer properties, thereby neglecting the interdependence of boundary layer development on the upstream body and the resulting change in fan inlet conditions [12] [13]. New approaches in performance quantification have been presented in recent years that analyze kinetic energy of the flow and mechanical power imposed on the flow, to identify and quantify sources and sinks of power along with their interactions rather than thrust and drag [14]. This results in an assessment of energy fluxes and dissipation rather than thrust and drag. However, to accurately achieve this comprehensive level of knowledge of the flow purely by experimental means alone is highly complex and prone to uncertainty [15]. Combining experimental and computational efforts to generate validated simulations is therefore of particular interest.

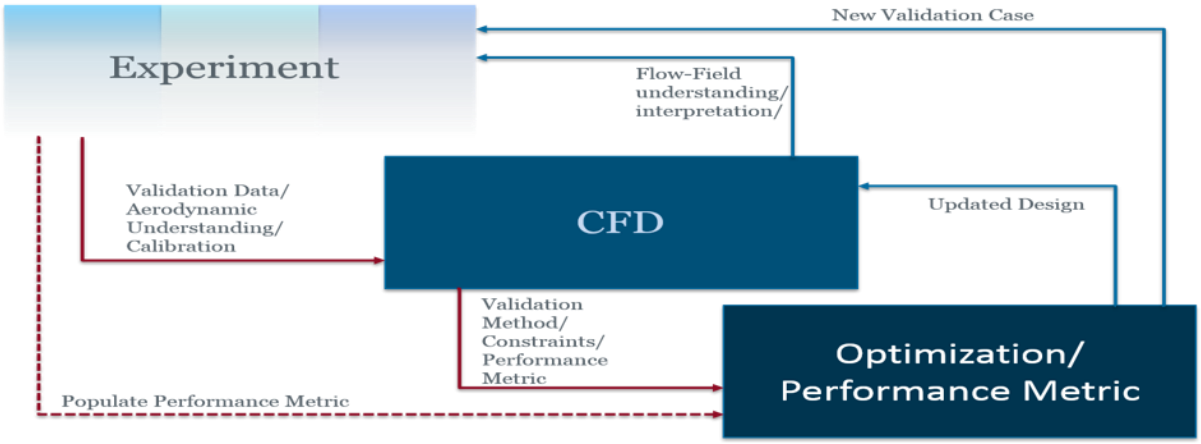

Fig. 1 Current research process illustration [16]

The current research process is outlined in Fig. 1 and consists of an iterative validation process, between experimental and computational techniques. Generation of high quality experimental datasets enable validation of computational methods and increases confidence in their use. The combined use of experimental and

computational approaches further underpin the development of suitable performance metrics for BLI configurations and subsequent performance optimization.

A modular low-cost experimental wind tunnel model has been developed that allows for parametric experimental investigation of various configuration options. In parallel, establishing validated computational models allows for deeper insights into the flow characteristics than can be readily measured in experiment. Modeling energy fluxes accurately by computation will allow for the application of alternative performance quantification techniques, together with subsequent system parametrization and design optimization. This paper presents details of recent experimental tests, together with ongoing validation studies for associated CFD simulations.

II. Experimental Study

This section will briefly describe the experimental wind tunnel model, experimental data acquisition as well as instrumentation. Further details on the design of the model and a presentation of an initial shake-down test can be found in [16].

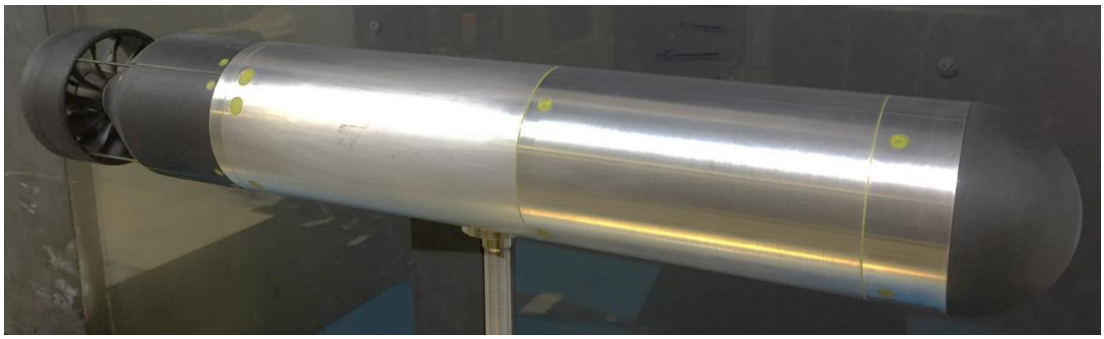

a) Full model

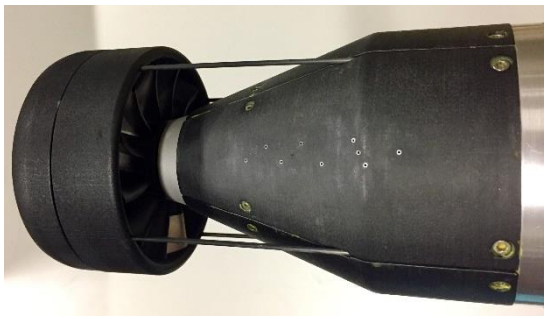

b) 20° Boat-tail angle

c) 30° Boat-tail angle

Fig. 2 Experimental model in Aero-Tunnel at University of Surrey

For the experimental investigation of a ducted fan in-line of an axisymmetric airframe, a modular wind tunnel model was developed and is shown in Fig. 2. The key aim for modularity was to retain maximum freedom for varying the configuration geometry in the vicinity of the boundary layer ingesting fan. This is crucial for the generation of various parametric datasets for the CFD validation process as well as subsequent optimizations. To provide modularity while being low-cost, the boat-tail geometry as well as the duct, stators and exit plug are 3D-printed from Nylon (PA2200) using selective laser sintering (SLS). The full model consists of a cylindrical body with a fineness ratio (L/D) of 6.6. The boat-tail aft-body houses a brushless DC-motor upstream of the fan. The current configurations investigated feature a straight boat-tail geometry at 20° and 30° as shown in Fig. 2b and 2c respectively with a 12 blade fan downstream of the boat-tail region. Both, motor and fan are commercially available low-cost components. Table 1 summarizes the key aspects of the experimental model setup.

L/D	Yaw (°)	Pitch (°)	Blockage (%)
6.6	± 5	± 10	~3.8

Table 1: Key details of the experimental wind tunnel model [16]

The experimental investigation was performed in the Aero-Tunnel at the University of Surrey. The closed-circuit tunnel features a 1.1m by 1.4m working section and flow velocities of up to 40m/s. The model was mounted via a cylindrical strut with a diameter of 0.2 of the diameter of the full model on a six-component force balance [17]. The force balance alongside ~2/3 of the strut were covered by a fairing. At its largest cross section, the model, strut and fairing result in a maximum tunnel blockage of ~3.8%.

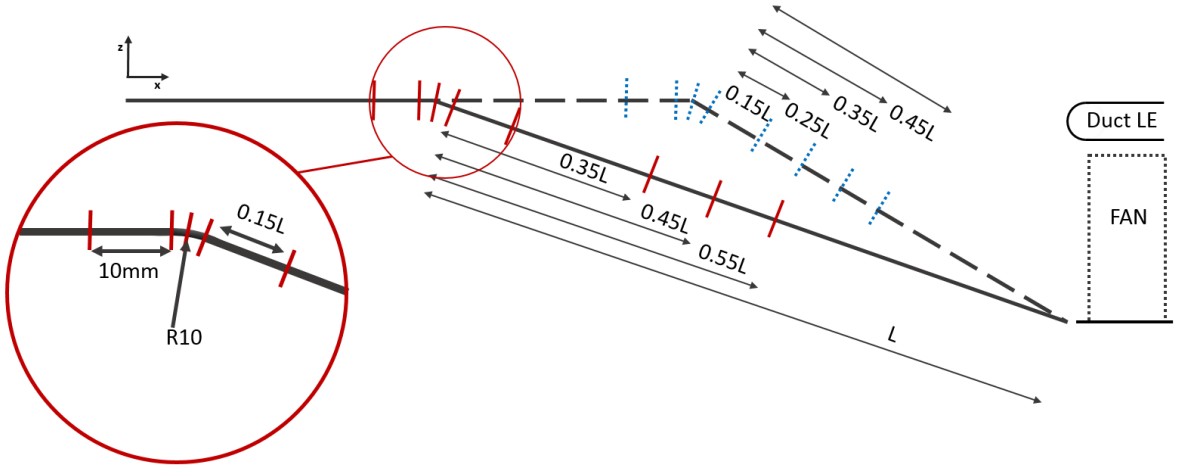

Fig. 3 Schematic of pressure taps for 20° and 30° configuration

The hemispherical nose of the model features 7 pressure taps at and around its stagnation point (akin to a 7 hole probe), which were used to confirm near-to-zero onset incidence test conditions. For the investigation of surface pressures upstream of the boundary layer ingesting fan, both boat-tail configurations were fitted with eight pressure taps, as shown in Fig. 2b and 2c. Figure 3 illustrates the surface pressure tap locations for which results will be presented later in the paper. In each case, the first pressure tap is located 10mm upstream of the start of the boat-tail, with 3 taps positioned at the start, center and end of the 10mm radius of curvature region. Internal packaging constraints associated with the presence of the motor within boat-tail region limited the placement of pressure taps close to the duct inlet. The remaining taps were hence located at 15%, 25%, 35%, and 45% of the length of the 30° boat-tail and at 15%, 35%, 45%, and 55% for the 20° boat-tail. The surface pressure taps were connected to eight-channel pressure scanners (Surrey Sensors Ltd. model ID8HP [18]) mounted inside the experimental model, having a full-scale range of 5 kPa and a total error band of less than +/- 0.5% FS.

Flow-field measurements were conducted using a two-component LDA system (Dante Dynamics [19]). A schematic of the model as well as the positions of flow field measurements is illustrated in Fig. 4. Measurements were repeated for both a vertical centerline plane and a horizontal centerline plane. A control volume was measured extending 2 diameters upstream, 4 diameters downstream and 3 diameters radially from the centerline. In order to capture the external flow physics effects of a boundary layer ingesting fan, four stations ahead of the fan as well as one station just downstream were measured. The stations are located at *i)* the beginning of the 3D printed aft-body, *ii)* at the start of the boat-tail region, *iii)* 30% down the length of the boat-tail as well as *iv)* upstream and *v)* downstream of the duct.

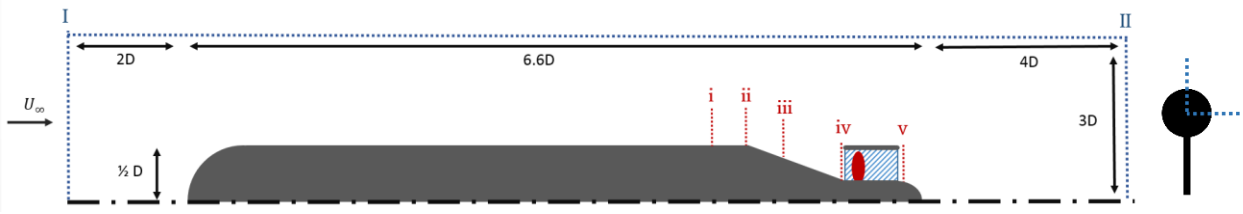

Fig. 4 Schematic of Experimental Model and LDA Measurement Planes

In addition to LDA measurements, a digital seven-hole probe system (Surrey Sensors Ltd. model ID7HP-050K [18] [20]) was used for downstream wake measurements at stations *v)* and *II* as well as 40 diameters downstream. The combination of multi-hole probe and LDA velocimetry allows for a more extensive investigation of the flow field. Furthermore, the seven-hole probe can measure all three velocity components. Figure 5 presents independent velocity component profiles at station *v)* taken by the seven-hole probe (7HP) and LDA. Since this is an axisymmetric model operated at zero incidence, results will be presented in terms of the axial velocity component (*u*), tangential velocity component (*v*), and radial velocity component (*w*).

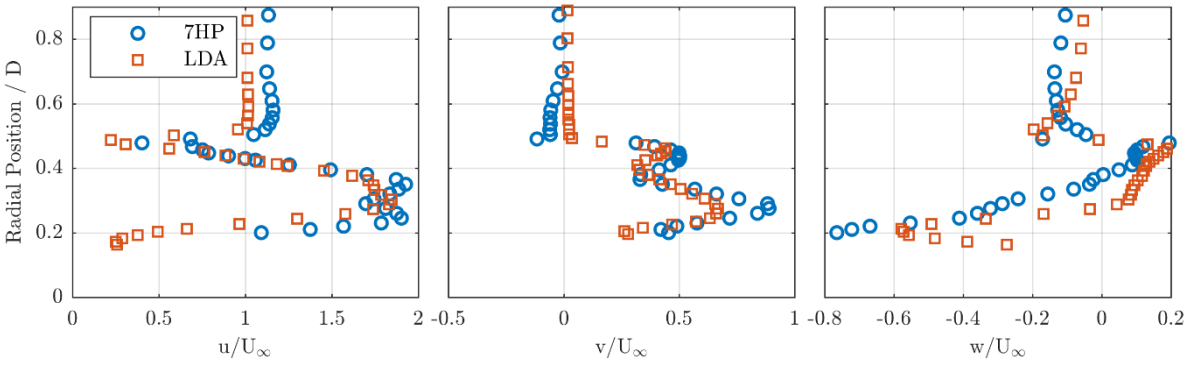

a) Axial velocity component **b) Tangential velocity component** **c) Radial velocity component**

Fig. 5 Velocity component profiles downstream of fan measured by LDA and 7-Hole-Probe at U_∞ = 30m/s

For the determination of the test conditions, a variety of different motor speed settings and their influence on surface pressures and model vibration were initially investigated. The electric motor is controlled by an electric speed controller (ESC) that measures the back electromotive force in order to calculate the motor speed. Critical fan speeds at which the model vibrates due to resonance were investigated. For certain fan speeds, model resonance associated with fan critical speeds was noted. Test conditions at speeds of 10000 RPM and 17000 RPM were chosen as suitable test conditions away from the region of resonance.

β	**Fan Speed (RPM)**						
	6000	**10000**	**11700**	**13000**	**16100**	**17000**	**18100**
20°	FB, C_p	FB, FF, C_p	FB, C_p	FB, C_p	FB, C_p	FB, FF, C_p	FB, C_p
30°	FB, C_p	FB, FF, C_p	FB, C_p	FB, C_p	FB, C_p	FB, FF, C_p	FB, C_p

Table 2: Test matrix of force balance (FB), flow field (FF), and pressure coefficient (C_p) measurements for boat-tail angle (*β*) and fan speed (RPM)

Table 2 outlines the test conditions investigated. The abbreviations FB refer to 6-component force balance data taken, C_p refers to surface pressures, whereas FF refers to detailed flow-field measurements using the aforementioned instrumentation. All test were conducted at a free stream velocity of 30 m/s corresponding to a

Reynolds number of 1.35×10^6. The values for surface pressure coefficients for the 30° configuration at varying fan speed are illustrated in Fig. 6.

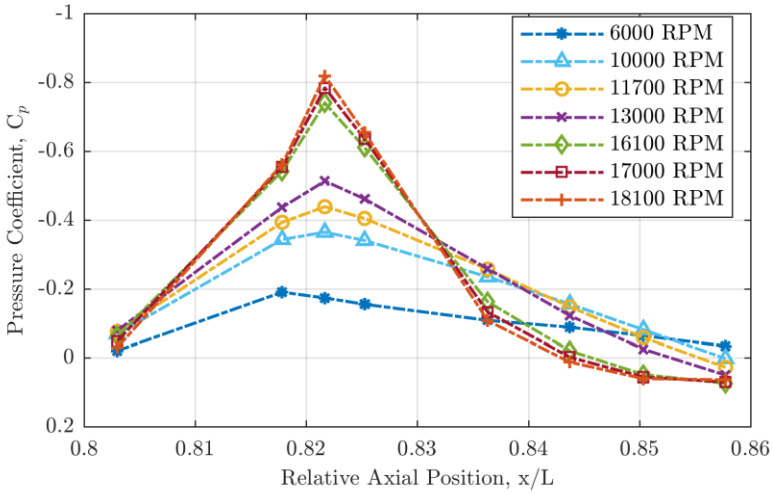

Fig. 6 Pressure Coefficient variation with RPM for 30° configuration

The reduction in the suction peak at the third measurement position is evident as speed reduces from 18100 RPM to 10000 RPM and has effectively vanished for the lowest RPM of 6000. Two test conditions at 10000 RPM and 17000 RPM were chosen based on the investigated model vibrations and surface pressures to further analyze the flow field and state of the boundary layer in greater detail and for initial CFD comparison.

The electric motor used was mounted on a metal bulkhead to ensure passive cooling. For each test condition the motor temperature was measured at three separate stations on the motor surface, as well as the ESC on its surface. To minimize any temperature dependent effects on the performance of the electrical components as well as magnets inside the motor [21], a steady-state temperature was achieved before flow field velocimetry data was taken. Reaching temperature equilibrium required ~30 minutes on average.

III. CFD Method

CFD results have been generated for the boundary layer ingesting fan configurations previously presented (Table 2). A structured mesh of the quarter body has been developed using ANSYS ICEM 17.2. The mesh consists of 3.3×10^6 cells that extend 20 diameters upstream and 40 diameters downstream of the model. ANSYS FLUENT 17.2 was used to provide incompressible RANS solutions using the k-ω SST turbulence model. Convergence was reached after 300-500 iterations on average, which was achieved in <1 hour on a high-spec desktop machine. Tunnel inflow boundary conditions defined the inflow velocity in the axial direction to match experimental conditions. The tunnel has been modeled with inviscid walls (no-slip not imposed). Rotational periodicity was used to capture three dimensional swirl effects. Viscous-scaled near-wall grid spacing on the body's surface was in the order of $Y_+ \approx 1$ for all simulations. Figure 7 shows the mesh around the full configuration, while Fig. 8 presents details of the mesh around the propulsion system at a) upstream and b) downstream locations.

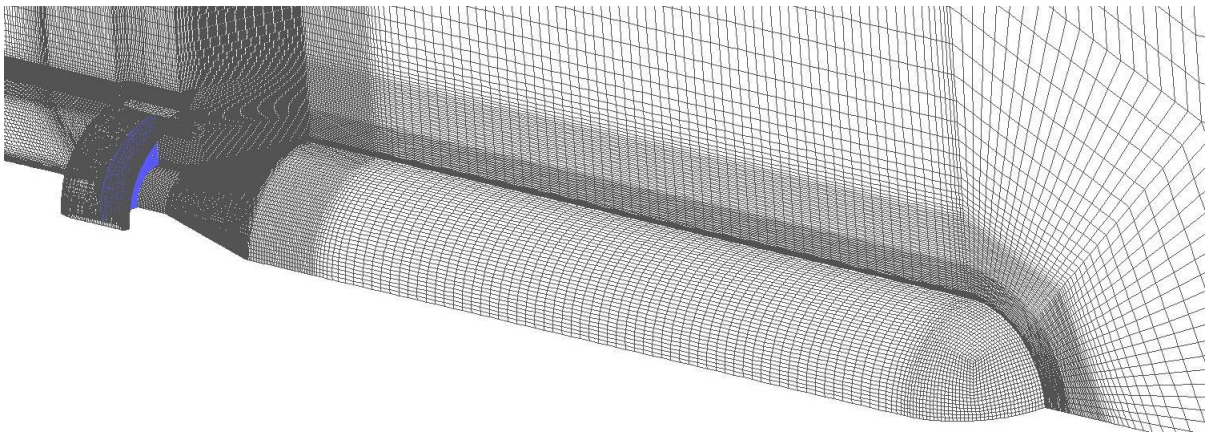

Fig. 7 Structured mesh of quarter-body

In order to retain reasonable computational cost per simulation, the fan is not modelled directly and instead is replaced by fan inlet and outlet faces. The boundary conditions applied on these inlet and outlet faces were derived based upon the experimental velocity component profiles. Furthermore, with the aim of eventually developing design guidelines for this type of propulsion system installation, a parameterized expression for these boundary conditions is desired.

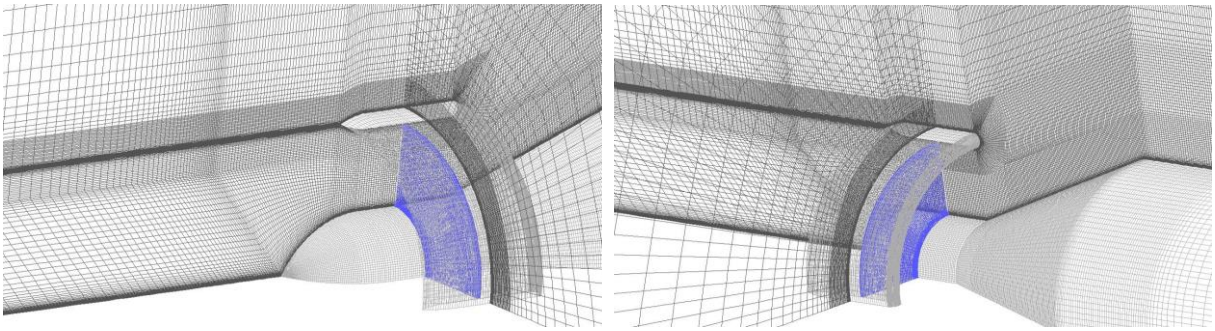

a) Downstream **b) Upstream**

Fig. 8 Structured mesh around propulsion system and fan face with vertical plane

A velocity inlet and outlet boundary condition is defined inside in the central region of the duct, outlined in blue in Fig. 8. The boundary condition for the fan inlet face is derived from the upstream experimentally measured velocity component profiles at station *iv* (Fig. 4). The fan outlet face on the other hand is based on the experimentally measured velocity component profiles at station *v* (Fig. 4). Three dimensional blade element theory is then applied to derive independent fan inlet and outlet boundary conditions, while retaining continuity.

The streamtube massflow is calculated from the experimentally measured profile downstream of the fan. The streamtube's edge is defined by the axial velocity component's minimum, situated on the lower edge of the wake of the duct's trailing edge. With the remaining velocity components downstream from LDA and seven-hole-probe measurements, a streamtube mass flow rate is calculated and the upper edge for the corresponding streamtube upstream of the fan consisting of the same mass flow is defined. Experimental investigations of the tangential velocity component upstream of the fan showed values of <1% of the free stream velocity. The streamtube upstream is therefore assumed to consist only of axial and radial velocity components. The resulting velocity profiles of the streamtubes from experiment are interpolated to have a constant radial distance in between the streamlines using a shape-preserving piecewise cubic interpolation polynomial. Figure 9 shows the derivation process of the boundary conditions from experimental measurements for one operating condition. *EXP US* refers to experimentally measured profiles at the upstream station *iv*, *EXP DS* to the profiles measured at the downstream station *v*. *Fan In* and *Fan Out* refer to the velocity components of the derived boundary conditions, for the fan inlet and outlet faces respectively, applied at the duct centre station. The applied method will likely over predict the velocities due to losses associated with turbulence and wall interaction being neglected.

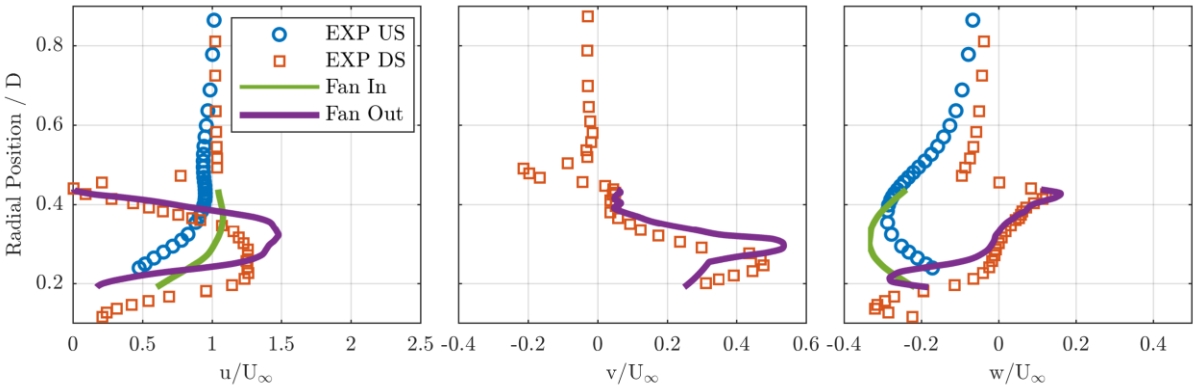

a) Axial velocity component **b) Tangential velocity component** **c) Radial velocity component**

Fig. 9 Derivation process of fan inlet and outlet boundary conditions from experiment

IV. Results

The key aim of this paper is to show the work undertaken to generate validated flow simulations at minimal computational cost for the eventual aim to parameterize the flow conditions for this type of propulsion installation. CFD results have been generated for the four cases previously presented in Table 2, corresponding to the RPM of 10000 and 17000 for the two configurations. The velocity magnitude ($\sqrt{u^2 + v^2 + w^2}$) has been multiplied by $u/|u|$ to also include the direction of the flow and capture potential separation.

Figure 10 and 11 show the comparison of the different speed settings at station *i*, the beginning of the 3D-printed aft-body piece, for the 20° and 30° configuration respectively. For both figures, it can be seen that the flow over the body does not present noticeable effects due to the change in fan speed. Both figures however show an underestimation of the local free stream velocity between experiment and CFD. This underestimation requires further investigation, but is believed to potentially be associated with experimental blockage affects which are not currently modelled in CFD. In particular, wind tunnel model mounting fairings are not currently included in CFD and, in addition, the tunnel walls are currently modeled with inviscid wall boundary conditions as opposed to a no-slip condition. In both figures the boundary layer thickness appears to be slightly reduced in CFD compared to experiment.

Figure 12 and 13 present results for the next downstream station ii, close to the start of the boat-tail region, where it can be seen that throttle dependent effects (sensitivity to fan speed) become more evident, particularly for the 30° configuration. The shape of the profiles has changed compared to the previous station, with a definite peak velocity region emerging. This change is caused by the upstream entrainment effect of the fan accelerating the upstream flow into the fan inlet. The sensitivity to fan speed, combined with the upstream entrainment effect of the fan, is captured reasonably well by CFD.

Figures 14 and 15 present results for station *iii*, 30% down the length of the boat-tail surface. The 30° configuration has a peak velocity which is ~5-10% higher than the 20° configuration. This is likely to result from the fact that the effective inlet area, between the boat-tail and the duct, is reduced for the 30° case, leading to increased mean flow speed to maintain mass flow into the fan. Again CFD captures the mean features associated with changing fan speed for both boat-tail configurations. Detailed analysis of the experimental results in Fig 15. indicate reversed flow and separation for the low fan speed condition, while the CFD results suggest reversed flow and separation for both fan speeds.

The profiles at station *iv*, shown in Fig. 16 and 17, are located just upstream of the ducted fan inlet, as shown in Fig. 4. For the higher fan speed in particular, the upstream acceleration of the flow due to the fan is apparent. The 30° lower speed case exhibits the largest deviation between experiment and CFD, particularly in the region close to the surface (Fig. 17), where CFD indicates recirculation and separation, as seen previously in Fig. 15. For the 30° higher fan speed case, for which CFD had indicated separation for the preceding station (Fig 15), there are no longer clear signs of separation, suggesting reattachment of the flow ahead of the fan. The challenging nature of accurately modeling flow separation and reattachment, through solution of the RANS equations with a k-ω SST turbulence model, has been observed in previous studies [22] [23].

The efflux profiles at station *v* are presented in Fig. 18 and 19. The wake from the duct can be seen at a radial position of approximately 0.5D and outside of this region the flow is external to the duct. The peak velocity in the efflux increases significantly with increasing fan speed. Comparing CFD and experiment, peak velocities are generally over predicted by CFD. In addition, the shape of the fan exit flow and the change due to fan speed is very similar for the two boat-tail angles, while there is a more significant variation seen in the CFD predictions. This could be a consequence of the differences seen earlier for separation predicted by CFD, but this requires further investigation and consideration in terms of how the fan boundary conditions are modelled. Overall, the approach taken for modelling the fan in CFD shows promise, based upon the qualitative agreement between CFD and experiment.

The surface pressure coefficients over the aft-body are compared in Fig. 20 and 21. Pressures from CFD agree well with experiment for the 20° case, over the entire range of the measured locations for both fan speeds. In addition, Fig. 20 shows that for the higher fan speed case, CFD predicts a noticeable adverse pressure gradient followed by a favorable pressure gradient along the boat-tail leading up to the fan, however this is not confirmed by experiment due to a lack of coverage in the pressure tap locations. For the 30° configuration in Fig. 21, there is good agreement in terms of the upstream pressures and suction peak. Downstream of the suction peak there is more deviation between CFD and experiment, with CFD indicating separation occurs on the boat-tail for both fan speeds. This is consistent with the results discussed earlier for Fig. 15 and 17. The 30° boat-tail configuration clearly represents a demanding flow case, which requires further investigation and modelling improvements.

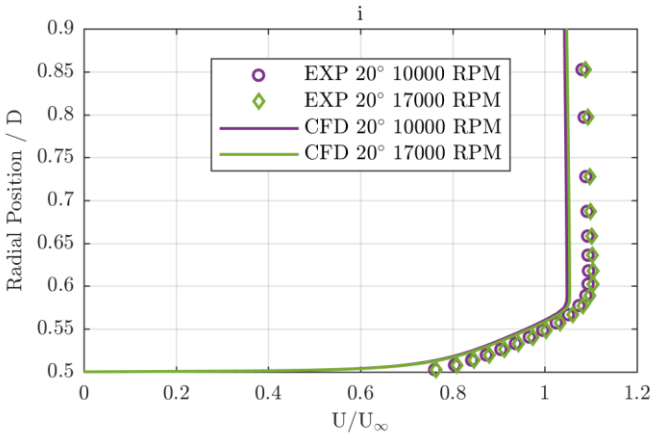

10) Velocity Profiles of 20° Boat-tail Angle at Station i

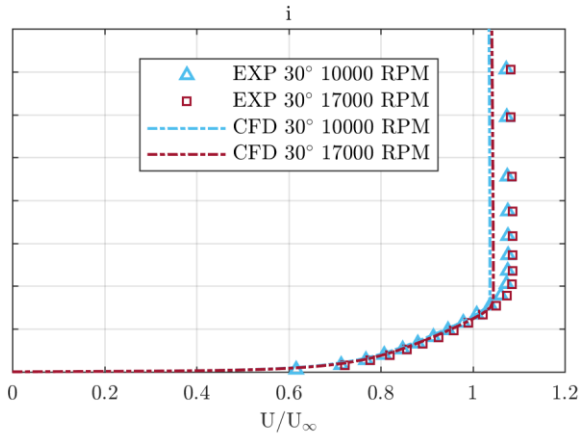

11) Velocity Profiles of 30° Boat-tail Angle at Station i

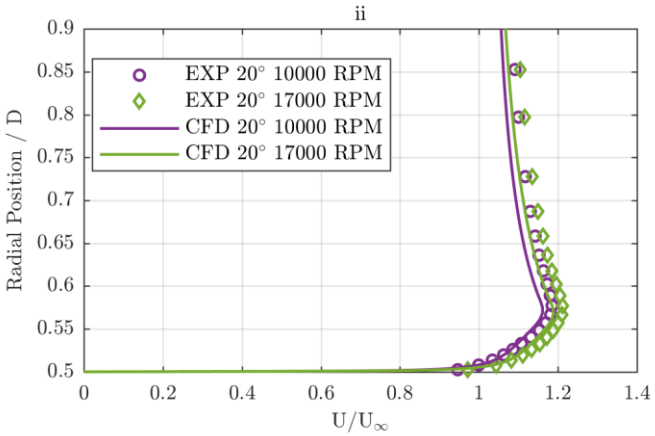

12) Velocity Profiles of 20° Boat-tail Angle at Station ii

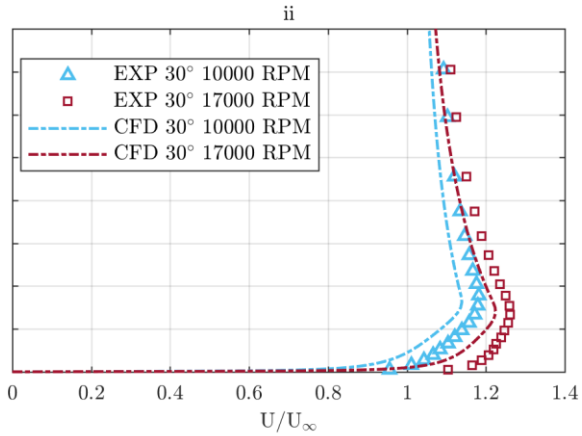

13) Velocity Profiles of 30° Boat-tail Angle at Station ii

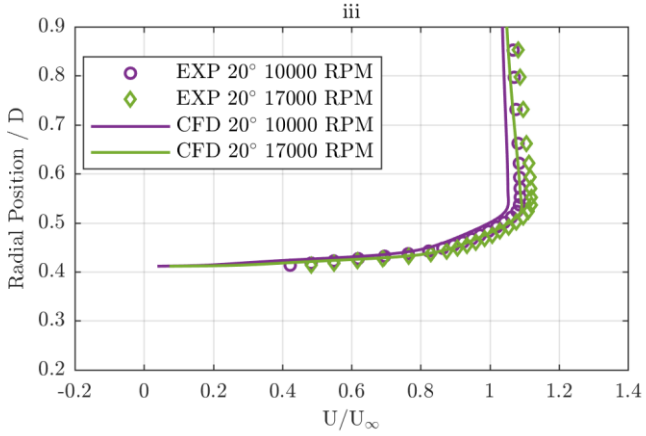

14) Velocity Profiles of 20° Boat-tail Angle at Station iii

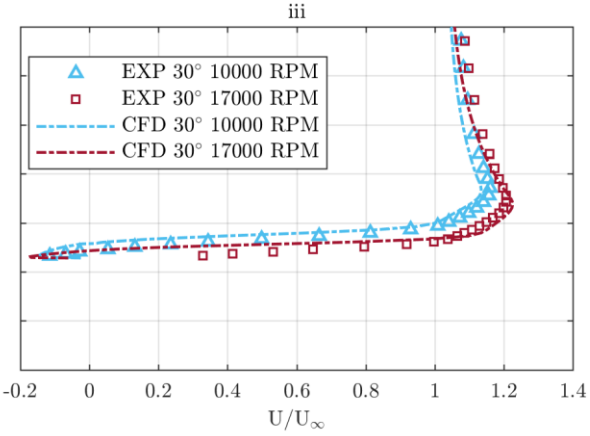

15) Velocity Profiles of 30° Boat-tail Angle at Station iii

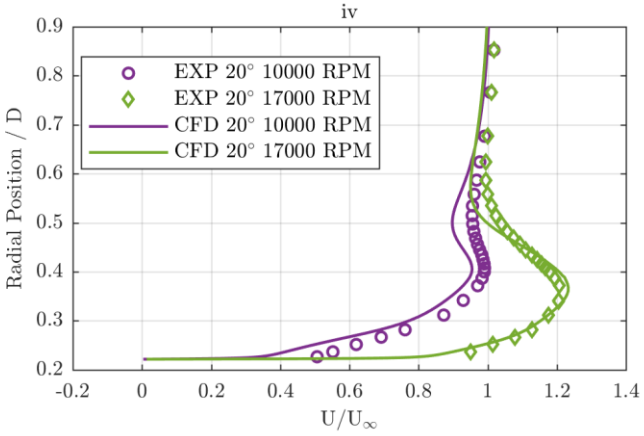

16) Velocity Profiles of 20° Boat-tail Angle at Station iv

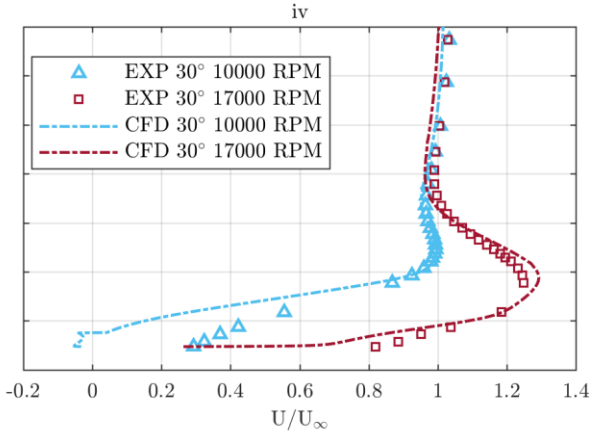

17) Velocity Profiles of 30° Boat-tail Angle at Station iv

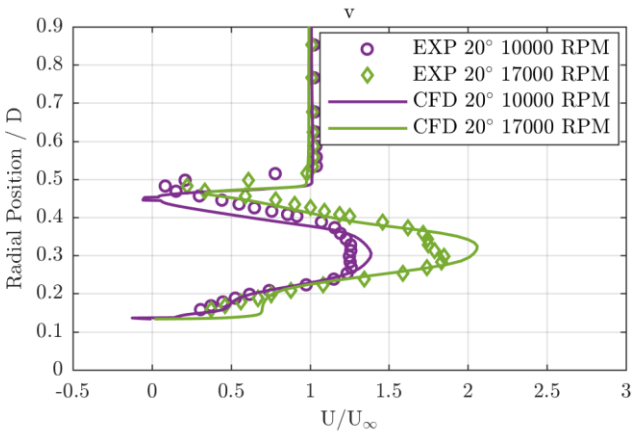

18) Velocity Profiles of 20° Boat-tail Angle at Station v

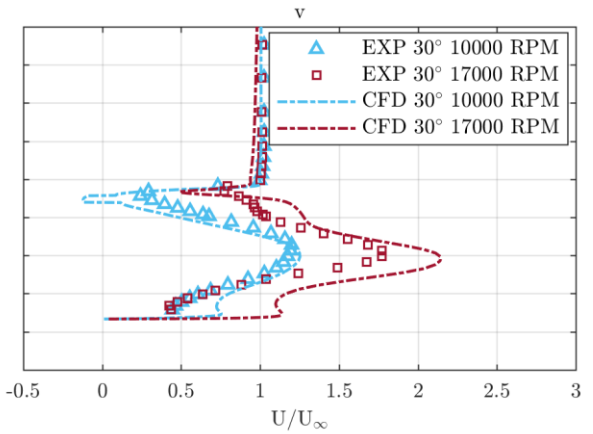

19) Velocity Profiles of 30° Boat-tail Angle at Station v

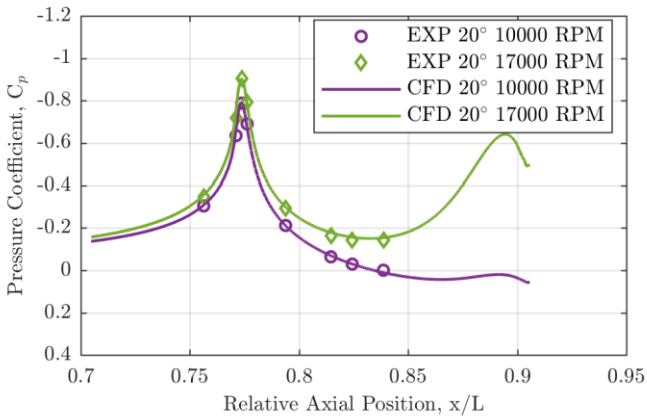

20) Pressure Coefficient on 20° Boat-tail

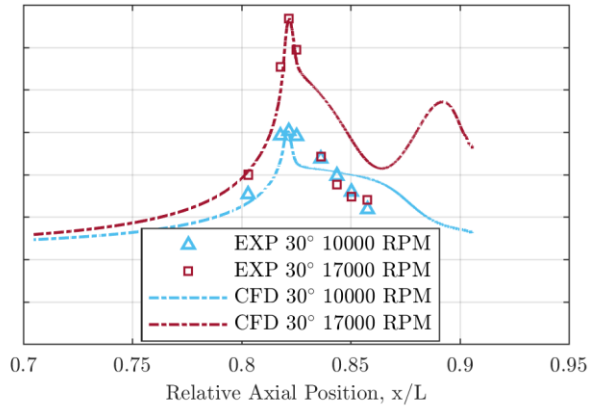

21) Pressure Coefficient on 30° Boat-tail

V. Concluding Remarks

Work towards CFD modelling and validation for an aft-body, in-line mounted, boundary layer ingesting, electric ducted fan, propulsion system has been presented. Details of a modular wind-tunnel model have been presented, for which parametric variation of the propulsion system can be investigated. Two boat-tail configurations, having high taper angles of 20° and 30°, have been analyzed by both experimental and computational means. The variation in fan speed for each configuration has also been investigated. A means for efficiently modelling the fan in CFD, using inlet and exit face boundary conditions, has been presented.

Comparison between CFD and experiment was generally good, particularly for the lower boat-tail angle configuration and for attached flow conditions. CFD predicts the effect of varying fan speed reasonably well, in terms of the flow and boundary layer growth seen over the upstream body and boat-tail. The simplified modelling of the fan has been shown to give promising results and the computational cost of the CFD calculations is relatively small, opening the opportunity for future use in direct design optimization studies. However, the current modelling does show limitations, in terms of predicting early onset of separation compared to experiment for the most challenging flow case associated with the 30° boat-tail at low fan speed.

Acknowledgments

The work presented has been carried out as part of a PhD research project funded by QinetiQ and the UK Engineering and Physical Sciences Research Council (1846031).

References

[1] L. Smith, "Wake ingestion propulsion benefit," *Journal of Propulsion and Power,* vol. 9(1), pp. 74-82, 1993.

[2] W. J. Rankine, "On the mechanical principles of the action of propellers," *Transaction of the Institute of Naval Architects,* 1865.

[3] G. W. Wislicenus., "Hydrodynamics and propulsion of submerged bodies," *ARS Journal,* pp. 1140-1148, 1960.

[4] W. S. Gearhart and R. E. Henderson., "Selection of a propulsor for a submersible system," *Journal of Aircraft,* pp. 84-90, 1966.

[5] A. Betz and W. Albring, "Introduction to the Theory of Flow Machines," *Journal of Applied Mathematics and Mechanics,* 1967.

[6] A. Fage and H. E. Collins, "An investigation of the mutual interference of airsrew and bodies of the 'pusher' type," *Advisory Committee for Aerodnautics,* 1917.

[7] A. Fage, Airscrews in Theory and Experiment, London: Constable & Company Ltd., 1920.

[8] H. Glauert, Airplane Propellers, Springer, 1935, pp. 169-360.

[9] E. M. Greitzer, P. A. Bonnefoy, E. D. Blanco, C. S. Dorbian, M. Drela, D. K. Hall, R. J. Hansman, J. I. Hileman, R. H. Liebeck and J. Lovegren, "N+ 3 aircraft concept designs and trade studies, final report volumes 1 and 2," *Rep. CR—2010-216794, NASA, Hampton, VA,* 2010.

[10] R. T. Kawai, D. M. Friedman and L. Serrano, "Blended Wing Body (BWB) Boundary Layer Ingestion (BLI) Inlet Configuration and System Studies," *NASA Contract Report, 214534,* 2006.

[11] A. Urangan, M. Drela, E. Greitzer, D. Hall, N. Titchener, M. Lieu, N. Siu, C. Casses, A. Huang, G. M. Gatlin and J. Hannon, "Boundary Layer Ingestion Benefit of the D8 Transport Aircraft," *AIAA Journal,* vol. 55, no. 11, 2017.

[12] C. Liu, G. Doulgeris, P. Laskaridis and R. Singh, "Thermal cycle analysis of turboelectric distributed propulsion system with boundary layer ingestion," *Aerospace Science and Technology,* vol. 27, no. 1, p. 163–170, 2013.

[13] J. L. Felder, H. D. Kim and G. V. Brown, "Turboelectric distributed propulsion engine cycle analysis for hybrid-wing-body aircraft," in *47th AIAA aerospace sciences meeting*, 2009.

[14] M. Drela, "Power balance in aerodynamic flows," *AIAA Journal,* vol. 47(7), pp. 1761-1771, 2009.

[15] P. Lv, D. Ragni, T. Hartuc, L. Veldhuis and A. Rao, "Experimental investigation of the flow mechanisms associated with a wake-ingesting propulsor," *AIAA Journal,* pp. 1-11, 2017.

[16] L. L. Kob, J. J. Doherty and J. Tolhurst, "Aerodynamics of an In-Line Boundary Layer Ingesting Electric Ducted Fan," in *Royal Aeronautical Society - The Future of Aerodynamics*, 2018.

[17] Aerodynmaic Test Equipment Ltd., "6 Component Force Balance SN0651 Calibration Report," Ate-Ltd., 2010.

[18] "Surrey Sensors," Surrey Sensors Ltd., 2019. [Online]. Available: http://surreysensors.com/. [Accessed 07 05 2019].

[19] Dante Dynamics, "Fibreflow Optics for LDA and PDA," Dante Dynamics.

[20] S. Shaw-Ward, A. Titchmarsh and D. Birch, "Calibration and use of n-hole velocity probes," *AIAA Journal*, vol. 53, no. 2, pp. 336-346, 2014.

[21] T. Sebastian, "Temperature effects on torque production and efficiency of PM motors using NdFeB magnets," *IEEE Transactions on Industry Applications*, vol. 31, no. 2, pp. 353-357, 1995.

[22] F. Menter, M. Kuntz and R. Langtry, "Ten Year of Industrial Experience with the SST Turbulence MOdel," *Turbulence, Heat and Mass Transfer*, vol. 4, 2004.

[23] V. Krishnan, K. Squires and J. Forsythe, "Prediction of Separated Flow Characteristics over a Hump using RANS and DES," in *AIAA Flow COntrol COnference*, Portland, Oregon, 2004.